POLITECNICO DI TORINO
Repository ISTITUZIONALE

Synthesis of tailored nanostructured gold surfaces for SERS applications by controlled seed deposition and growth

Terms of use:

Publisher copyright

(Article begins on next page)

03 September 2025
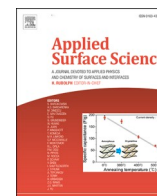
Full Length Article

Synthesis of tailored nanostructured gold surfaces for SERS applications by controlled seed deposition and growth

Matteo Giardino [a], Ilaria Mannelli [b], Renwen Yu [c], F. Javier García de Abajo [b,d], Valerio Pruneri [b,d], Davide Janner [a,*]

[a] Department of Applied Science and Technology and RU INSTM, Politecnico di Torino, Corso Duca degli Abruzzi 24, 10129 Torino, Italy
[b] ICFO-Institut de Ciencies Fotoniques, The Barcelona Institute of Science and Technology, Castelldefels 08860 (Barcelona), Spain
[c] Department of Electrical Engineering, Ginzton Laboratory, Stanford University, 94305 Stanford, California, USA
[d] ICREA-Institució Catalana de Recerca i Estudis Avançats, 08010 Barcelona, Spain

ABSTRACT

Surface-enhanced Raman spectroscopy (SERS) sensors are commonly based on metal nanoparticles in colloidal suspension followed by deposition on a substrate. Despite its simplicity, this approach leads to non-uniform SERS substrates that are hampered by features such as coffee rings. Seed-mediated growth starting from nanoparticles already deposited on a flat substrate potentially allows for creating more uniform and reliable sensors. However, the deposition process, the control of the distribution of the seed nanoparticles, and their optimal growth have not been thoroughly explored. In this work, we present a systematic approach to designing and fabricating gold nanostructured surfaces, tailoring their SERS responses on demand. By controlling and tuning the deposition of nanoparticles, assisted by an experimental and theoretical investigation, we achieved good control over the spatial distribution of the deposited seeds. After enlarging such seeds through chemical reduction, the optimized SERS substrates show great uniformity in their hotspots, a critical feature for sensors. The so-fabricated substrates were used for detecting Skatole in water, achieving a detection limit of 42.2 ppt. The developed methodology has significant implications for the advancement of several fields, particularly SERS-based sensing, enabling the design and targeting of specific excitation wavelengths and Raman bands while obtaining uniform and reliable substrates.

1. Introduction

Raman vibrational spectroscopy has been widely employed in many analytical chemistry[1,2] and bio-analytical applications,[3,4] especially in fields requiring high chemical specificity due to the unique fingerprint each molecule shows in its Raman spectrum.[5] The main drawback of Raman spectroscopy lies in its small scattering effects cross-section, which reduces its detection efficiency and sensitivity. Nonetheless, the Raman scattering intensity can be increased by orders of magnitude by leveraging the plasmonic field enhancement of noble metal nanostructures[6,7] as in Surface-Enhanced Raman Spectroscopy (SERS), which allows the detection and characterization of a tiny number of molecules bound or close to the metallic surfaces, down to the single-molecule level[8–11]. This is due to the local fields that are enhanced far more when neighboring nano-features interact over distances of the order of a few nanometers.[12–15] Regions of a highly enhanced local electromagnetic field are called hotspots. Because of the strong dependence of the SERS enhancement on the substrate that gives rise to this effect, many years of research have been devoted to creating and optimizing SERS substrates to provide the largest enhancements possible and increase hotspot density.[16–22]

SERS structures can be roughly classified into three categories: metal nanoparticles (MNPs) in suspension,[23] MNPs immobilized on solid substrates,[24] and nano-structures fabricated directly on solid substrates, including nano-structures obtained by nanolithography and templating.[25–28] Despite all of the SERS advantages and the advancements in fabrication techniques, the ubiquitous use of SERS remains challenging due to the lack of commercially available, reproducible, highly sensitive, and uniform substrates. Nowadays, only a few substrates are available on the market (e.g. Q-SERS™, SERS Vials™, Renishaw™), and among them, Klarite®, commercialized by Renishaw, is the most known and frequently used as a reference for the
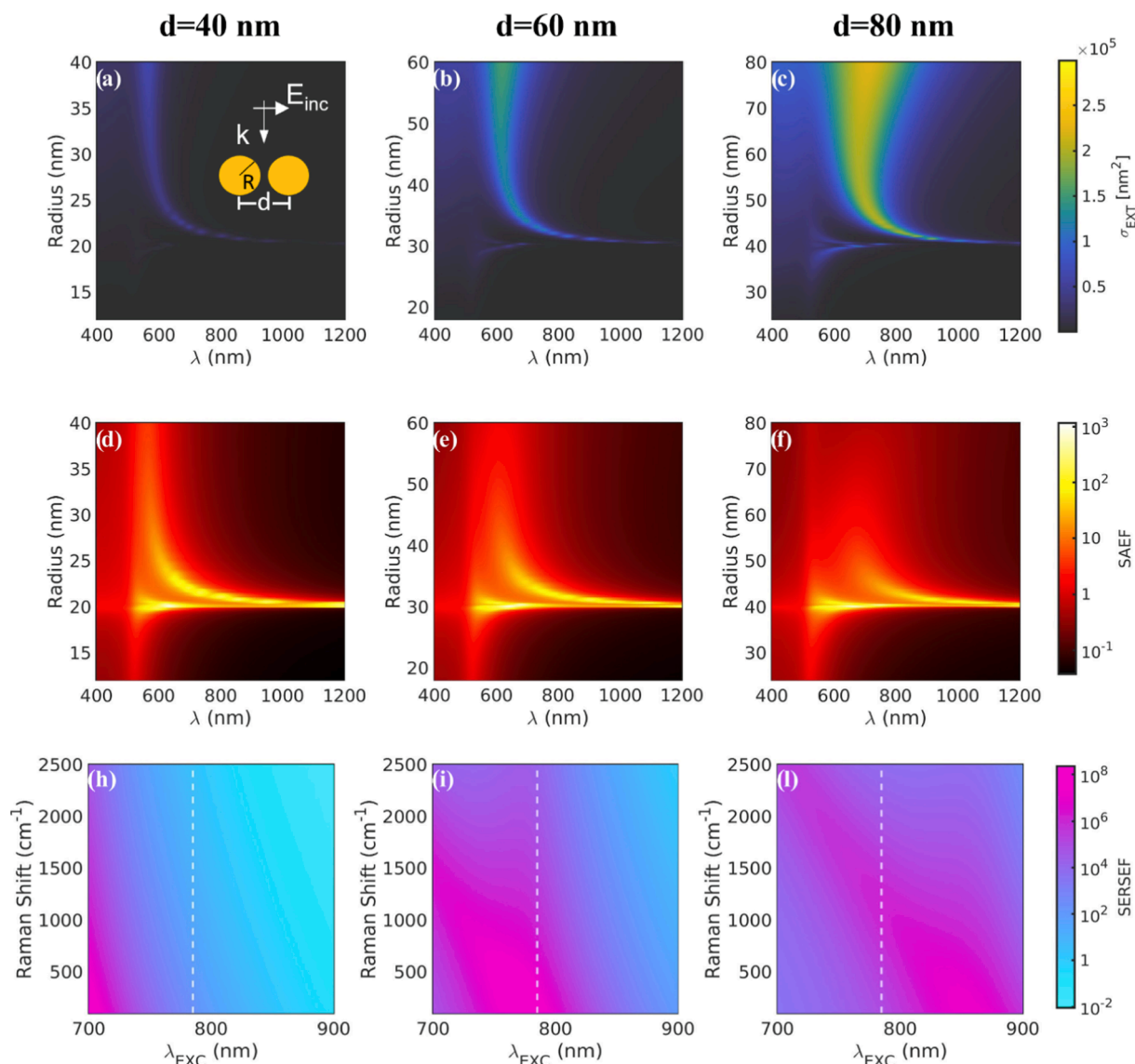
Fig. 1. Upper plots: Extinction cross sections of gold dimers as a function of wavelength and particle radius for different center-to-center distances $d = 40$ nm (a), 60 nm (b), and 80 nm (c). Middle plots: Surface-averaged field intensity enhancement (SAEF) due to the excitation of plasmonic resonances in gold dimers as a function of wavelength and particle radius for different center-to-center distances $d = 40$ nm (d), 60 nm (e), and 80 nm (f). Lower plots: SERS enhancement factor (SERSEF) in gold dimers as a function of excitation wavelength and Raman shift for different center-to-center distances $d = 40$ nm (g), 60 nm (h), and 80 nm (i). The particle radius is set to $a = d + 2$ nm in all cases. The white dashed lines indicate the 785 nm excitation wavelength used in this work.

characterization of new substrates.[29,30].

Recently, different types of hydrophobic and superhydrophobic patterned structures for SERS application were developed[31,32]. These are of utmost importance when working with highly diluted solutions as they allow us to concentrate the analyte at specific points of the substrate where the Raman measurement is performed[31]. ome fabrication approaches based on nanoparticle agglomeration [33] were investigated to obtain more uniform SERS responses leading to promising results for the detection of molecules at ultralow concentration. However, both the hydrophobic and the agglomeration approaches rely on further processing steps with respect to a simple deposition making the overall procedure more complex. Actually, the fabrication of uniform and efficient SERS substrates remains challenging because of the complex fabrication process and high cost. Designing and fabricating SERS substrates with a simple method that provides a much more uniform hotspot formation while retaining high enhancement factors could boost the practical usage of this analytical tool.

Different works have focused on studying optimized nanoparticle

arrays for SERS applications. Felidj et al.[34] observed that optimal results were achieved for particle size and shape that give a plasmon resonance at a wavelength that is located between the wavelength of the laser excitation and that of the Raman band under consideration. Joseph et al. studied[35] the effect of particle diameter on the SERS enhancement factor in gold nanoparticle (NP) arrays and concluded that large nanoparticles showed higher enhancement. Their study, however, was limited only to particles with a diameter in the range 15—40 nm. On the other hand, Hong and Li[36] experimentally studied the detection of 4-aminothiophenol and 4-nitrotiophenol in water with Au-NPs-based SERS sensor and observed that the highest enhancement of the Raman signal is obtained for nanoparticles whose diameter lies in the range between 50 and 60 nm.

More recently, Pal et al. investigated[37] the effect of particle size and separation distance on SERS enhancement factor (SERSEF) in gold and silver nanoparticle arrays. They observed a positive linear correlation with the nanoparticle size and a negative exponential relation with the interparticle separation distance. However, they hypothesized these

trends could be attributed to the higher scattering cross-sections offered by bigger particles and the higher density of hotspots obtained with small separation distance, but their sensor was prepared by dewetting a gold thin film, and therefore they could not obtain particles with separation distance lower than 20 nm.

The deposition of gold nanoparticles from a colloidal suspension onto a functionalized substrate represents a facile and effective way to obtain a highly uniform substrate and offers the possibility of controlling the average center-to-center distances. So far, different works have studied[38] this problem by adopting an Extended Random Sequential Adsorption (ERSA) model, and the results were in good agreement with the experimental results[38,39]. However, to the best of our knowledge, this adsorption theory has not been used to optimize nanoparticle deposition for SERS substrates, particularly to control the average distance between the nanoparticles.

Leveraging on a theoretical and experimental optimization for the deposition process, in this study, we propose a method to obtain highly optimized and uniform SERS substrates based on a Grown Nanostructured Surface (GNS) that consists of a monolayer of gold nanoparticles assembled on a previously functionalized surface and successively grown to obtain a hotspot enriched surface to boost the Raman signal intensity.

A preliminary theoretical analysis and ERSA simulations assisted in obtaining optimal conditions and guidelines for the fabrication process (i.e., optimal average distance and growth conditions of the nanoparticles). As a SERS response test and to verify the uniformity of the signal over the substrate, a monolayer of 4-mercaptobenzoic acid was used. To test the optimized GNS SERS substrate on a practical industrial application, Skatole (3-methylindole) was chosen. Skatole is a volatile compound associated with unfavorable odors and flavors in pork meat, most commonly known as boar taint.[40] For this chemical, the accepted threshold levels are in the range of 0.5—1 μg per gram of fat (equivalent to roughly 1.8—3.6 μM)[5,41] and, at present, its quantification is only realized by chromatography techniques, with limits of detection (LODs) in the range of 4—500 ng/g.[42,43] The study of the analytical performances of the substrate, made by detecting Skatole at low concentrations, and the comparison with the commercially available Klarite, demonstrate that the fabricated substrates achieve high and uniform sensitivity across our SERS substrate, reaching a detection limit down to the part-per-trillion level.

2. Materials and methods

2.1. Optical response of non-percolated gold nanoparticles

We use the Maxwell-Garnett (MG) effective medium theory[44,45] to describe the optical response of a metamaterial layer composed of non-percolated gold nanoparticles on top of a silica substrate. The effective permittivity of such metamaterial is given by

$$\epsilon_{\text{MG}} = \epsilon_s \frac{2f_1(\epsilon_{\text{Au}} - \epsilon_s) + 2\epsilon_s + \epsilon_{\text{Au}}}{2\epsilon_s + \epsilon_{\text{Au}} + f_1(\epsilon_s - \epsilon_{\text{Au}})},$$

where f_1 is a fitting parameter characterizing the filling factor of gold, ϵ_{Au} is the permittivity of gold taken from experimental data,[46] and $\epsilon_s = (\epsilon_{\text{silica}} + 1)/2$ is the average permittivity of the surrounding media, with $\epsilon_{\text{silica}} = 2.13$. We find $f_1 = 0.03$ for Fig. 1b and $f_1 = 0.05$ for Fig. 1c to compute the absorption spectra of initially deposited nanoparticles with an averaged lateral size of 10 nm.

2.2. Optical response of percolated gold nanoparticles

Gold nanoparticles start to percolate during the nanoparticle growth process, and the MG effective medium theory is no longer accurate. Instead, we use Bruggeman's effective medium theory,[44,45] in which the permittivity ϵ_B of the metamaterial is determined from the relation

$$(1 - f_2)\frac{\epsilon_s - \epsilon_B}{\epsilon_s + 2\epsilon_B} + f_2\frac{\epsilon_{\text{Au}} - \epsilon_B}{\epsilon_{\text{Au}} + 2\epsilon_B} = 0,$$

where f_2 is the gold filling factor in the percolated region. Furthermore, a mixture of percolated and non-percolated nanoparticles exists in our samples. Therefore, we adopt an effective permittivity as a combination of MG and Bruggeman's effective medium theories,[45]

$$\epsilon_{\text{eff}} = F\epsilon_B + (1 - F)\epsilon_{\text{MG}},$$

where F indicates the weight of each region. For the metamaterial on APTMS-functionalized substrate, we find $f_1 = 0.18$ (0.17), $f_2 = 0.18$ (0.165), $F = 0.68$ (0.88), and an averaged nanoparticle lateral size of 35 nm (40 nm) to calculate the absorption spectra for the sample after 180 s (210 s) growth. As for the metamaterial on DETA-functionalized substrate, we find $f_1 = 0.08$ (0.048), $f_2 = 0.14$ (0.128), $F = 0.35$ (0.45), and an averaged nanoparticle lateral size of 30 nm (35 nm) to calculate the absorption spectra for the sample after 120 s (150 s) growth.

2.3. Far- and near-field properties of particle dimers

The far- and near-field properties of particle dimers in a vacuum are simulated by using the boundary-elements method (BEM) available through the Matlab-based tool MNPBEM[47]. The dimer is excited by normal-incident plane wave radiation whose polarization is directed along the dimer axis. Optical data for gold is taken from Johnson and Christy[46].

To take into account the field-enhancement properties of the dimer, the Surface Averaged Enhancement Factor (SAEF) was calculated as the mean over the dimer surface Σ of the square modulus of the normalized electric field $\frac{E(\lambda)}{E_0}$.

$$SAEF(\lambda) = \frac{1}{\Sigma} \oint_\Sigma \left| \frac{E(\lambda)}{E_0} \right|^2 d\Sigma$$

Moreover, to better compare the SERS response of different dimer systems, a SERS Enhancement Factor (SERSEF) was defined as the product between the SEAEF at the laser exciting wavelength λ_{EXC} (785 nm) and the SAEF at a wavelength $\lambda_{EXC} + \Delta\lambda_{RS}$ corresponding to a Raman shift $\Delta\lambda_{RS}$:

$$SERSEF(\lambda_{EXC}, \Delta\lambda_{RS}) = SAEF(\lambda_{EXC}) \cdot SAEF(\lambda_{EXC} + \Delta\lambda_{RS})$$

2.4. Modeling of gold nanoparticles deposition

Gold nanoparticle deposition has been modeled using an extended random sequential adsorption (ERSA) simulation.[38] The interaction potential W_{pp} of two charged particles of radius a at a distance d is given as

$$W_{pp} = Z\exp[-\kappa(d - 2a)]$$

where κ is the Debye Length and Z is a constant defined as

$$Z = 2\pi a\varepsilon_0\varepsilon_r\zeta_p^2$$

The Debye Length κ for the nanoparticle suspension in citrate was estimated to be 14.1 nm. The hydrodynamic radius a_H and zeta potential ζ_p of the NPs were measured with a Malvern Zeta Seizer Nano. The suspension's pH was measured by a commercial pHmeter as 6.41. The zeta potentials ζ_{APTMS} and ζ_{DETA} of both APTMS- and DETA-functionalized glasses at the same pH value were measured with an Anton Paar Surpass 3 instrument and are $+30.9$ and $+26.7$ mV, respectively. Since the particles and the glass substrates are charged with opposite signs, the adsorption probability term W_{ps} due to particle–substrate repulsion was set equal to 1. The simulation was conducted at 298 K on a square glass substrate of size 10 μm by 10 μm. Water viscosity at 298 K was assumed

equal to $\mu_w = 9.16 \cdot 10^{-4}$ Pa·s;[48] water relative dielectric constant at the same temperature was assumed equal to $\varepsilon_r = 78.54$. For each of the three simulation runs, the nearest neighbor distribution has been calculated as follows:

$$d_{NN}(r, \delta r) = \frac{1}{N} \sum_{i=1}^{N} \lambda_i(r, \delta r)$$

where N is the total number of particles and λ_i is equal to 1 if the distance between the $i-$th particle and its nearest neighbor lies between r and $r + \delta r$ or 0 otherwise, namely:

$$\lambda_i(r, \delta r) = \begin{cases} 1, r \leq |\overrightarrow{x}_i - \overrightarrow{x}_{NN}| < r + \delta r \\ 0, \qquad\qquad \text{otherwise} \end{cases}$$

The nearest neighbor distributions were fitted with a Gaussian curve by a least square procedure, and the center of the fitting Gaussian has been considered as the average nearest neighbor distance $\langle d_{NN} \rangle$.

2.5. Surface preparation

The SERS-active substrates were fabricated on fused silica surfaces. Substrate cleaning was performed by ultrasound treatment in acetone (10 min), ethanol (5 min), detergent (MicroSoap for 10 min), and milliQ H$_2$O (5 min) and dried with a N$_2$ stream. Before the functionalization step, an O$_2$ plasma activation was carried out (50 W power for 5 min). The functionalization was realized by coating with two different amino-silanes for comparison: (3-aminopropyl)trimethoxysilane (APTMS) 97 %, and N$_1$-(3-Trimethoxysilyl-propyl)diethylene-triamine (DETA) from Sigma-Aldrich. The treatment aimed to obtain self-assembled mono-layers (SAM) of the two different silane. SAM formation was obtained by dipping the activated surfaces in ethanolic solutions of silanes for two hours with the following concentrations in %wt: 2.5 % APTMS and 4 % DETA. After functionalization, the substrates were removed from the solution, rinsed three times with ethanol, and sonicated in ethanol for 5 min. The samples were then blow-dried with N$_2$ and used immediately for Au nanoparticle deposition or stocked in a vacuum in a clean environment to preserve the quality of the functionalization.

2.6. Gold nanoparticles deposition and growth

The functionalized surfaces were coated with a monolayer of citrate stabilized 10 nm diameter Au nanoparticles by immersion in the nano-particle solution as received from the supplier Sigma-Aldrich ($\sim 6.0 \times 10^{12}$ particles/mL). After soaking the substrates in the nanoparticle solution in a closed container for 18 h, they were rinsed with milliQ H$_2$O and gently blow-dried with N$_2$. For the final SERS substrates fabrication, the seed nanoparticles immobilized on the surface were grown by immersing the substrates in an aqueous solution containing 0.28 mM HAuCl$_4$ and 1,75 % H$_2$O$_2$.[49] The growth reaction was carried out for the different amounts of time as detailed in the text and under vigorous magnetic stirring. The reaction was stopped by removing the substrate from the solution and rinsing it with abundant milliQ water. The substrates were then used for SERS measurements or stored under vacuum in a clean environment to prevent contamination

2.7. Surface characterization

Topological analysis of the substrates was realized by atomic force microscopy (AFM) with the digital instrument D3100 AFM. Character-ization of the substrate before and after functionalization with amino-silanes was measured in tapping mode to control the roughness before and after the process. After deposition and growth of the nanoparticles, the substrates were characterized by topography and lateral force AFM measurements realized in contact mode.

The lateral force AFM images were processed, identifying the grown

particles detected by their border as a change in the force (see fig. S11). The barycenter of each grain was considered as the center of the deposited particle. Statistics of the correlation of the center-to-center distance $D(x)$ between the particles were calculated and fitted with the following distribution:

$$D_{fit}(x) = A(x - x_0) e^{-\frac{(x-x_0)^2}{2\sigma^2}} \, for \, x \geq x_0,$$

and for $x < x_0$ we assume $D_{fit} = 0$. SEM images of the grown nano-particles were taken by a FE-SEM Scanning Electron Microscopy (FEI Inspect F) at an acceleration voltage ranging from 5 kV to 20 kV. Absorbance spectra of the substrates were recorded with a Spectrometer UV/VIS Lambda 950 (PerkinElmer) in a wavelength range from 400 nm to 850 nm. More details can be found in SI 5.

2.8. SERS measurements

The quality and homogeneity of the substrates were evaluated by measuring the Raman signal produced by a molecule monolayer covering the grown particles. In this case, the signal intensity is directly related to the hotspot density per unit surface. All SERS measurements were performed using the Renishaw inVia Raman Microscope with a laser excitation wavelength of 785 nm, a typical power of 100 μW, 10 s integration. Normalization of the counts was obtained following the formula:

$$P_{norm} = \frac{P_{meas}}{NA \cdot T_{int} \cdot N_{acc} \cdot P_{ex}},$$

where P$_{meas}$ is the signal as measured by the instrument, NA is the nu-merical aperture of the objective used, T$_{int}$ is the integration time in seconds, N$_{acc}$ is the number of accumulated spectra, and P$_{ex}$ is the power of the excitation laser. SERS signals were recorded from different points, and around each point, a map of the signal was acquired, scanning surfaces of 50 μm^2 and 150 μm^2 with 50X (NA 0.75) and 20X (NA 0.4) objectives, respectively as indicated in the text. The results were compared with signals from the commercial Klarite substrate covered with an MBA monolayer under the same conditions.

Limits of detection (LOD) and limits of quantification (LOQ) were determined according to the International Conference on harmonization of technical requirements for the registration of pharmaceuticals for human use[50], namely:

$$LOD = \frac{3.3\sigma}{m}$$

$$LOQ = \frac{10\sigma}{m}$$

where m is the slope of the linear fitting of the calibration curve and σ is the standard deviation of the sensor SERS response.

3. Results and discussion

3.1. Surface analysis

In gold NP arrays, the enhancement of the SERS signal is mediated by the field intensity amplification provided by the localized surface plas-mon resonances (LSPRs) residing in the gold nanostructures, especially in the gaps or grooves. The nano-structure we propose in this study is composed of a random distribution of various gold spherical nano-particles with different lateral distances, the fundamental element of which is a gold dimer with radius a and center-to-center separation distance d, as illustrated in the inset of Fig. 1a.

Fig. 1a-c present the extinction cross-sections as a function of the wavelength and the particle radius for such gold dimers with different center-to-center separation distances. An abrupt change in the

Table 1
Measured hydrodynamic radius, zeta potential, concentration, and simulated average center-to-center distance for different Au NPs.

NPs diameter (nm)	a_H (nm)	ς_P (mV)	C_0 (10^{12}/mL)	$<d_{NN}>$ (nm)
10	7	−47.9	5.98	54.5
20	12	−50.8	0.65	80.7
40	22	−40.5	0.07	108.6

extinction spectra can be observed when the two spheres start to approach each other, which is a consequence of the classical electro-magnetic model we are using (more in Methods). Note that this phe-nomenon is a quantum effect due to electron smearing and tunneling between two spheres in the nearly touching regime (sub-nanometer gaps)[51] In the present work, we neglected such a nonlocal effect, as it is impossible to control the diameter of grown nanoparticles with such atomic-scale precision.

A redshift of the resonance can be seen for touching dimers of larger sizes. Correspondingly, as shown in Fig. 1d-f, the peak of the surface-averaged near-field intensity enhancement (more in Methods and Sup-plementary SI1-4) follows the trend of the extinction peak, the maximal value of which can be above 10^3 when the two spheres are just touching. As the particles continue to grow, the dimers start resembling larger oblate spheroidal nanoparticles and a blueshift of the extinction peak is therefore observed. Moreover, as the particles touch and form the dimer, a second absorption band associated with a transversal plasmon mode is observed towards the NIR region. As a result of the field intensity enhancement provided by those gold dimers, we find that, for an exci-tation wavelength of 785 nm, the surface-averaged SERSEF (see its

definition in Methods) can be amplified to a value of nearly 10^8 for a dimer of $a = 30$ nm and $d = 62$ nm, as shown in Fig. 1h. More generally, we observed that this dimer exhibits a SERSEF higher than 10^6 for all the Raman shifts in the range from 100 to 2500 cm^{-1}.

When the center-to-center separation distance d increases to 80 nm (Fig. 1i), the SERS signal gets weaker due to a degradation of the field intensity enhancement, as shown in Fig. 1e. Analogously, if the center-to-center distance is decreased to 40 nm (Fig. 1g) the SERSEF will decrease and achieve at values lower than 10^4.

It is also important to note that, when we explore the SERS signal from the collective response of more than two interacting nanoparticles, the maximal value of the surface-averaged SERS enhancement factor can be equally obtained by summing the contributions from individual di-mers, as shown in Figure S5. We therefore used the dimer as the fundamental constituting unit that can model with sufficient accuracy the optical response of Au NPs arrays. This fact allows us to find the peak value of the SERS signal by only investigating that from a single dimer.

3.2. Particle deposition simulation

It was already observed by Semmler et al.[52] that, in the diffusional adsorption of charged nanoparticles onto a functionalized surface, the maximum coverage factor mainly depends on the repulsive electrostatic interparticle interactions. These repulsive interactions, shown in the Methods section, are directly proportional to the particle radius. Grabar et al.[53], focusing on the kinetics of these adsorption processes, observed that, in the first stage of the deposition, the coverage factor is limited by diffusion, whereas at the equilibrium, the effect of repulsive
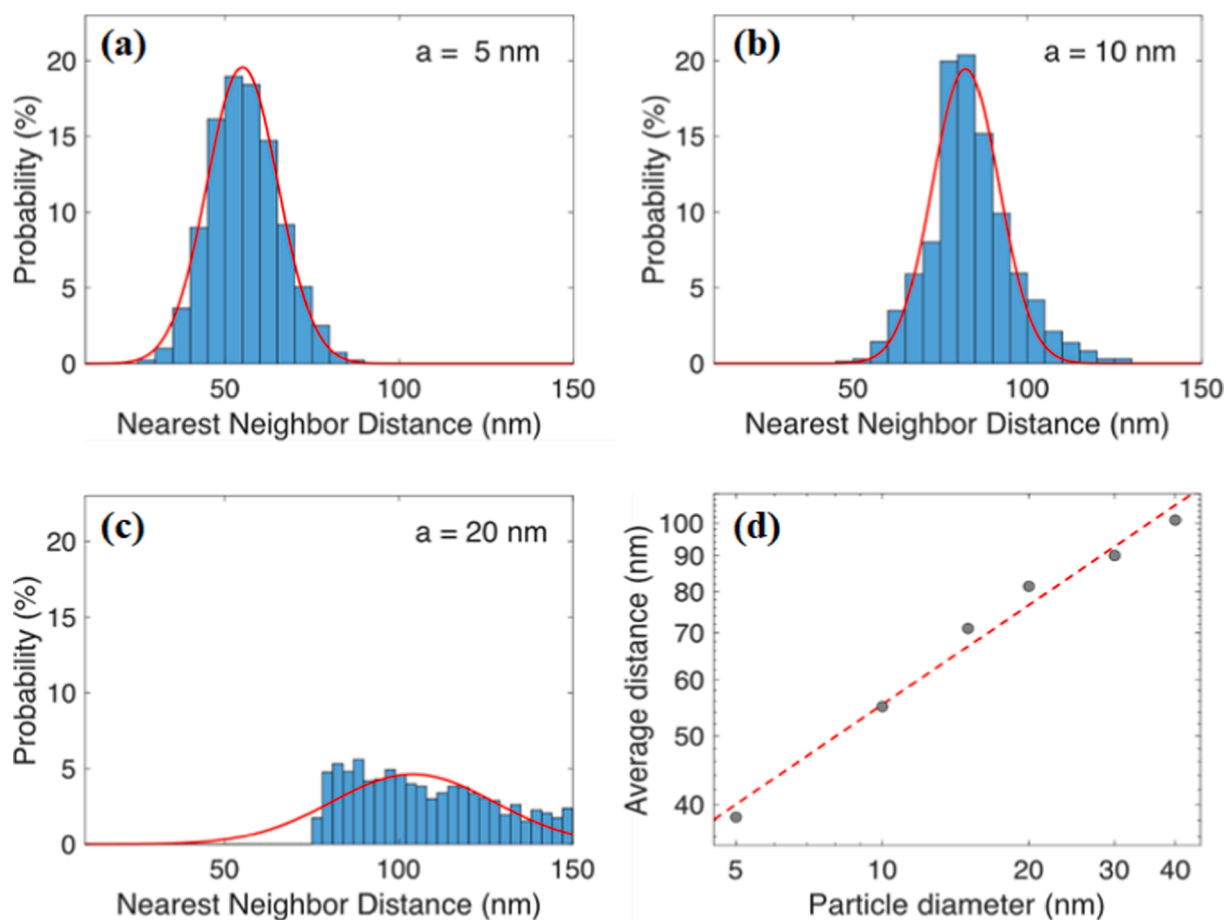

Fig. 2. Nearest-neighbor center-to-center distance for different seed nanoparticle radii: (a) 5 nm, (b) 10 nm, and (c) 20 nm. The histograms are fitted with a Gaussian distribution (continuous curve). (d) Correlation between particle diameter and average distance after a fixed deposition time (18 h) from ERSA simulations. The dashed line is a fit for the data points.
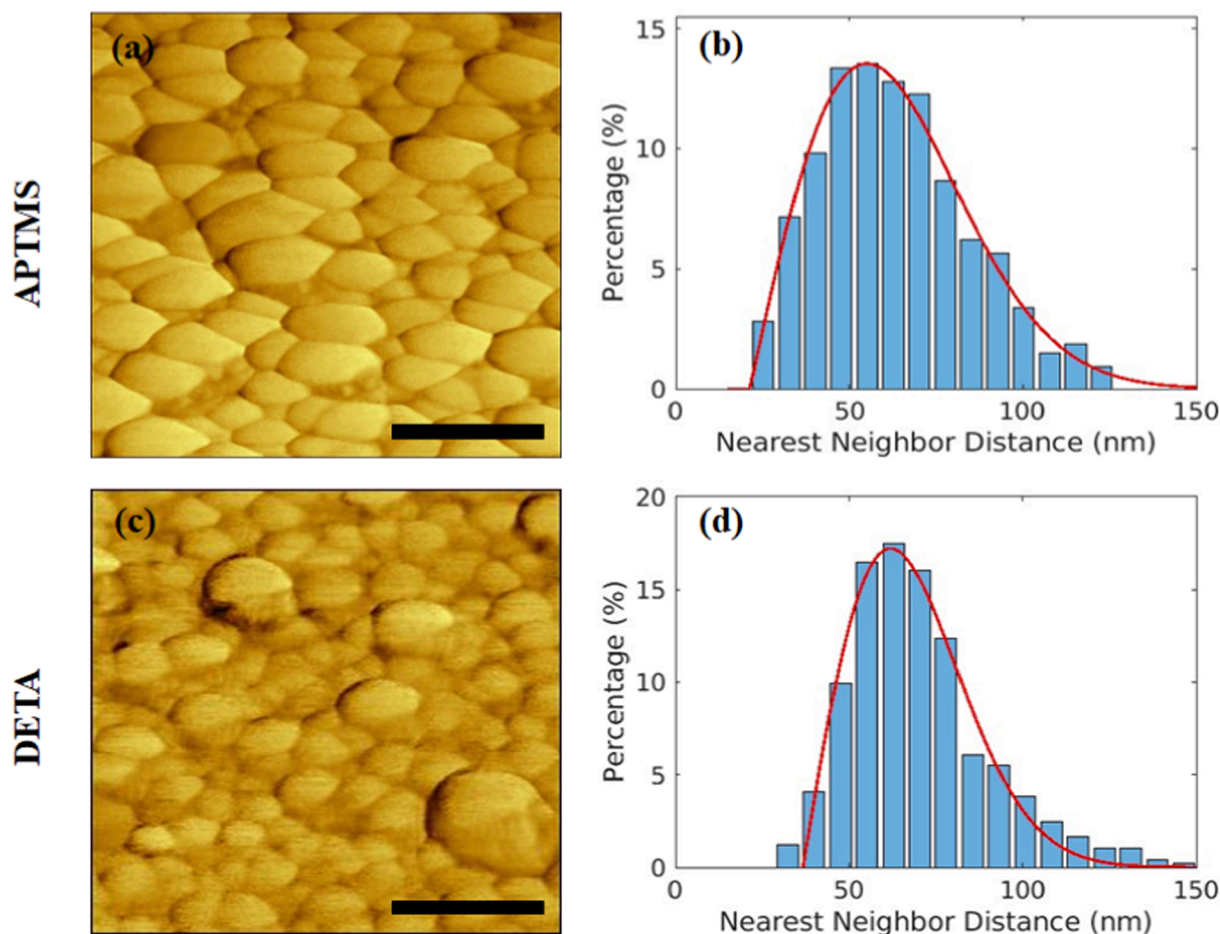
Fig. 3. (a) AFM topography (contact mode) and (b) nearest-neighbor distance distribution of the APTMS-functionalized GNS. (c) AFM topography (contact mode) and (d) nearest-neighbor distance distribution of the DETA-functionalized GNS. Center-to-center distance distribution for the nearest-neighbor histogram from shear AFM measurements and a Gaussian fitting of the distribution (red-solid curve). The scale bar in (a) and (b) is 200 nm.

interactions is strongly predominant.

According to these experimental observations, the process of particle deposition has been successfully modeled with the ERSA simulation scheme[38] that we used to study the deposition of gold seed particles on the silane-functionalized substrates as described in the Methods.

Particle deposition simulations are run in this work to identify the optimal conditions to obtain an average center-to-center distance approaching the optimal value of 60 nm obtained from the optical simulation. Three different types of particles with different nominal diameters (i.e. 10 nm, 20 nm, and 40 nm) are simulated to obtain the average interparticle distance that maximizes the enhancement factor at 785 nm. In the simulation of the deposition, time is set to 18 h to ensure the achievement of the maximum coverage factor for all three types of nanoparticle suspension. In particular, the analysis of average center-to-center distance is reported in Supplementary Sect. S4, and Figure S6 shows a favorable timing for 10 nm nanoparticles.

The hydrodynamic radius a_H, zeta potential ζ_p, and concentration C_0 have been measured for each particle type (see Table 1). Moreover, from the simulation results, the average nearest-neighbor center-to-center distance $\langle d_{NN} \rangle$ of each type of nanoparticles has been calculated and are reported along with the measured parameters in Fig. 2 and Table 1.

From these results, we can observe that the average center-to-center distance significantly increases with the radius of the seed nanoparticles. Among the three values of interparticle distance, the one which is closest to 60 nm, and therefore maximizes the SERSEF, is obtained by the deposition of the 10 nm gold seeds. For this reason, we focused on the fabrication of GNS using seeds of 10 nm to prepare the SERS substrates.

3.3. Control of the deposition of seed nanoparticles on the substrate

To obtain the optimized gold Grown Nanostructured Surface (GNS), we investigated the different steps involved in the fabrication, evaluating their impact on the SERS signal for a test monolayer of 4-mercaptobenzoic acid (MBA). The steps to obtain GNS substrates are three: functionalization of the substrate, gold seed deposition, and growth. According to the results of the ERSA simulation, a gold nanoparticle seed of nominal diameter 10 nm has been chosen and is employed in the rest of this study for substrate fabrication. As the glass substrate, we selected microscope slides with roughness < 2 Å to avoid a nano-texture that could favor aggregation or a 3D arrangement of the deposited seed nanoparticles. Indeed, the ideally flat surface, more easily enables the deposition of NP in a monolayer, allowing the assumption that the nanoparticle distribution occurs on a 2D surface randomly. The final aim is to obtain a specific distribution of seed nanoparticles with a controlled average distance between them. In such a case, it will be possible to obtain the desired density of hotspots by a controlled growth process of the seeds.

Functionalizing the substrate with different silane monolayers can change the coverage and density of particles on the surface. Indeed, at the equilibrium, there is a limit in deposition; Finegold et al.[54] demonstrated that the maximum coverage factor for randomly placed particles is 0.503. However, this maximum value is attained only if the particles are non-interacting with each other. Otherwise, the minimum distance between two adjacent particles can be affected, and a lower coverage factor is typically obtained.[55] A perfect silane monolayer
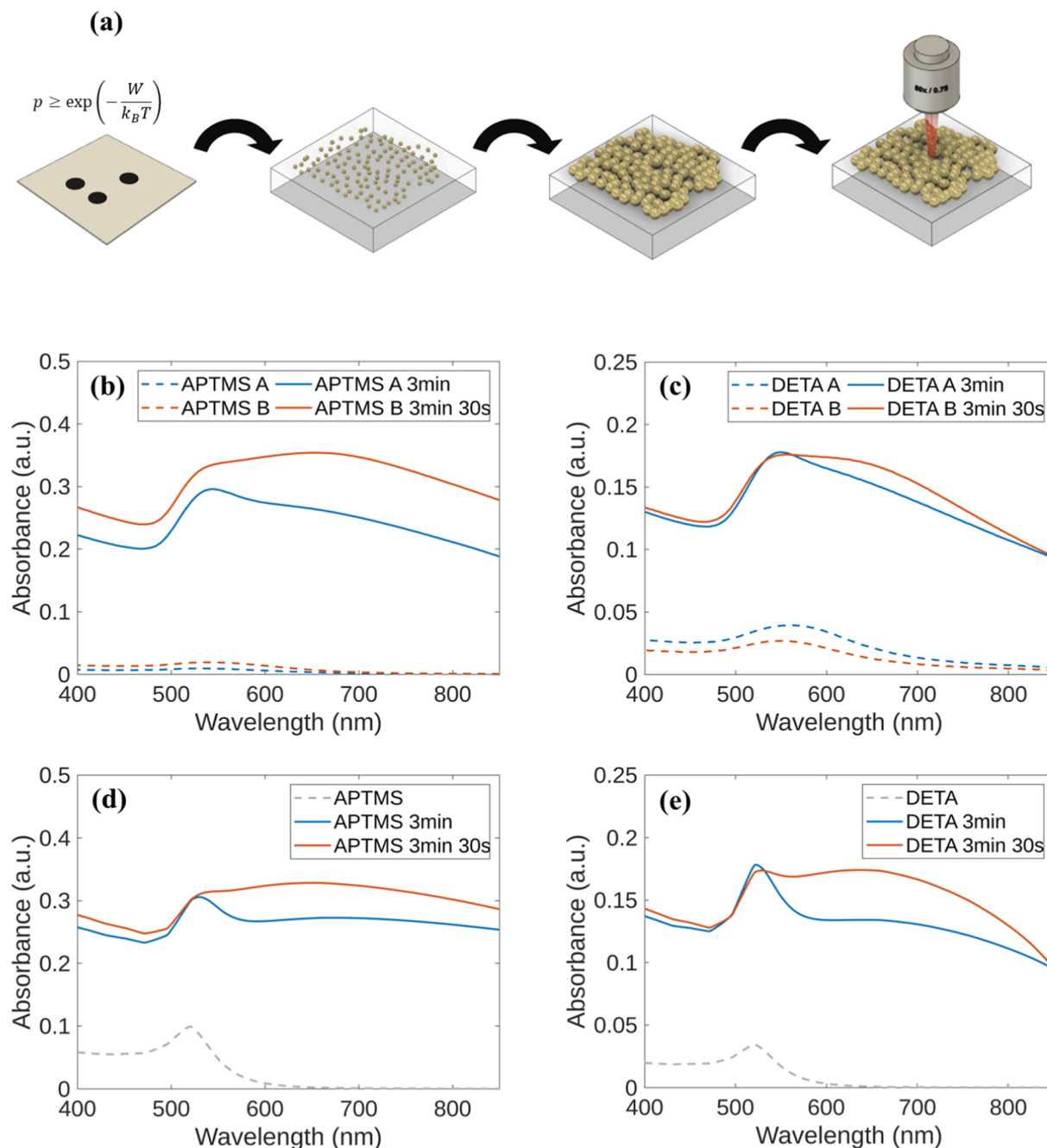
Fig. 4. (a) Fabrication process of SERS substrates from ERSA simulation to deposition of seed gold nanoparticles, and subsequent controlled growth to obtain SERS hotspots. Substrate absorbance of deposited nanoparticles on substrates functionalized with APTMS (b) and DETA (c) at as-deposited nanoparticles (dashed curves) and after growth (solid curves). Effective-medium-theory calculations for the growth of deposited nanoparticles on substrates functionalized with DETA (d) and APTMS (e) at as-deposited nanoparticles (dashed curves) and after growth (solid curves).

should cover the glass surface conformally, thus keeping the roughness unaltered. An increase in roughness value and the presence of debris on the surface could indicate an irregular coverage or the formation of micelles adsorbed on the surface. In our experiments, we used two different silanes terminated with amine groups such as (3-aminopropyl) trimethoxysilane (APTMS), and N_1-(3-Trimethoxysilyl-propyl)diethylenetriamine (DETA). It has been demonstrated by Sukham et al.[56] that aminosilanes constitute an excellent adhesion layer between gold and oxides, so that particles are strongly bonded to the substrate, making it suitable for SERS applications.

Initially, the quality of the functionalization coating made by treatment with silane has been studied by atomic force microscopy (AFM).

The arithmetic average of the roughness profile (R_a) after silane deposition is the same as observed on clean fused silica before the functionalization, 0.2 ± 0.1 nm, indicating that the silane coating has homogeneously covered the surface (Figure S7). The optimal concentrations for APTMS and DETA were chosen from the best results obtained with respect to the roughness. After functionalization, the 10-nm-nanoparticle-seed deposition was carried out starting from stock solutions as described in the Methods.

Among the particle diameters investigated through Monte Carlo simulations, 10 nm was chosen to obtain an average center-to-center distance that was closest to the optimal value of 60 nm obtained from the optical response simulation (i.e., 54.5 nm). For the deposition, we
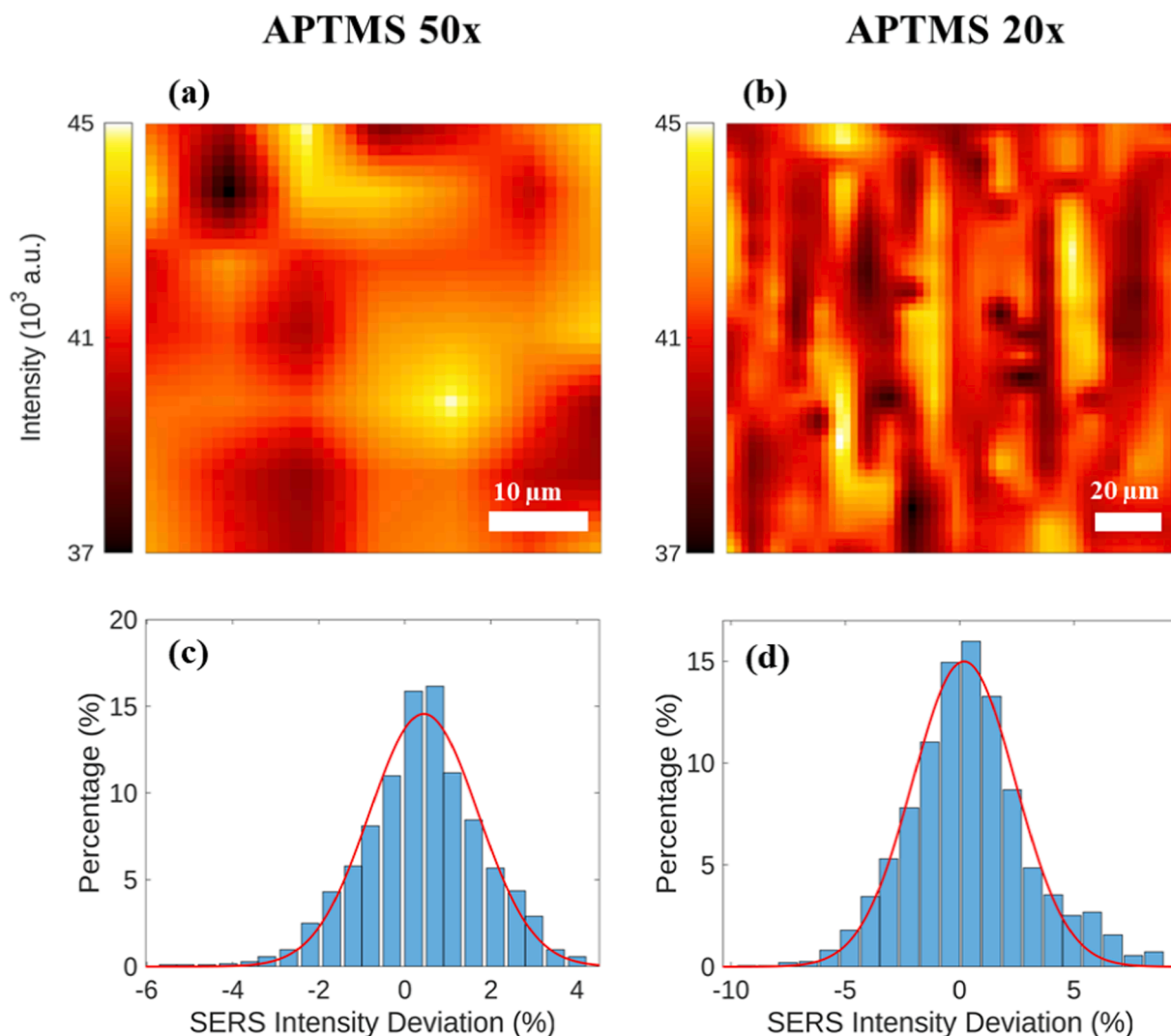
APTMS 50x
APTMS 20x

Fig. 5. Maps and histograms of the SERS peak signal at 1076 cm^{-1} for samples functionalized with APTMS. We report measurements taken with 50 × (a and c) and 20 × (b and d) objectives. The distribution histograms (c) and (d) are fitted with Gaussian functions (red-solid curves).

employed the Au nano seed colloidal suspension as provided by the supplier whose properties are reported in Table 1.

To be able to detect the center-to-center distribution, the deposited seeds were grown for 3 min, and AFM of the surfaces was taken in shear mode to better detect the crevices. The results from the AFM analysis are reported in Fig. 3 showing the center-to-center distributions considering the nearest neighbors as described in the Methods. From the figure is clear the influence of surface functionalization which affects the deposition with its surface potential. The peaks of the distances are 59 nm for APTMS and 65 nm for DETA.

3.4. Seed growth and substrate characterization

The process followed for the creation of the grown nanostructured surfaces is illustrated in Fig. 4a. Standard growth of nanoparticles was performed to increase the size of the nanoparticles in order to make them more clearly observable and ease the AFM and scanning electron microscope (SEM) characterization. Successively, the seed nanoparticle deposition and growth have been confirmed by measuring the absorbance spectra of the surfaces. Growing times from 30 s to 300 s have been used (Section S4 in SI). It has been extensively observed that the absorbance peak due to the plasmonic resonance of gold nanoparticles undergoes both a broadening and a redshift as the particle size increases. [57] Moreover, as the particles grow and the interparticle gaps decrease,

they start forming dimers, which can exhibit a longitudinal LSPR mode that may extend down to the NIR range (>700 nm).[58].

Fig. 4d-e show the absorbance spectra before and after the growth process. In this case, the used growing times were 210 s and 180 s for APTMS and DETA. It is clear that the larger dimensions of the nanoparticles enhance the scattering cross section, and therefore the absorbance intensity at the plasmon resonance peak increases from 0.02 AU to 0.35 AU. Moreover, a peak broadening is observed after growth, suggesting that the interactions within the nanoparticle plasmons are higher in this new distribution (in which the particles are touching) than before. A better understanding of the clustering between grown nanoparticles is obtained from the SEM measurements reported in the SI (Section S10), where one can see that the touching nanoparticles form crevices and hotspots with a high density on the substrate.

The analysis of the substrate homogeneity evaluated by coating the surface with an MBA self-assembled monolayer (SAM) is resumed for APTMS and DETA in Fig. 5. In this case, MBA was chosen as a model molecule due to its high Raman cross-section and its capability of strongly bonding to gold nanoparticles. The Raman spectrum has been recorded at a different surface point, and at each point, a signal map has been obtained using the measurements made in a nine-point matrix. The MBA spectrum is characterized by two main peaks at 1076 cm^{-1} and 1588 cm^{-1} respectively. The first peak is associated with in-plane aromatic ring breathing and asymmetric stretching $\nu(C - S)$, whereas the

Table 2

Comparison of relative deviation with respect to the average of the signal at 1077 cm^{-1} for the maps reported here and Klarite (ND: Not Detected).

	Substrate	σ (%)	3σ (%)
20x	APTMS	1.3	3.9
	DETA	2.2	6.5
	Klarite	3.1	9.3
50x	APTMS	3.06	9.17
	DETA	1.95	5.85
	Klarite	ND	ND

second is due to the symmetric stretching $\nu(C - C)$.[59] A deviation in SERS signal expressed in percentage with respect to the average of the measured area can be defined as:

$$S_{dev}(x,y) = \left(\frac{S(x,y)}{\langle S(x,y) \rangle_{Area}} - 1 \right) \times 100$$

where $S(x,y)$ is the peak SERS signal at 1076 cm^{-1} at point (x,y), $\langle S(x,y) \rangle_{Area}$ is the average of the signal S over the entire area, and S_{dev} is the percentage deviation from that average value. Fig. 4 shows the Raman map made over an area of 150x150 μm^2 and constructed using the signal of the MBA peak at 1076 cm^{-1} or 1588 cm^{-1}.

Moreover, we have compared the results with the commercial Klarite substrate from Renishaw (Table 2). Klarite substrates were less uniform in terms of SERS Signal Intensity if compared to the substrates produced in the frame of this work. The different silanization also affected the substrate uniformity. When using a 20x objective, the APTMS substrate shows a lower standard deviation on the SERS intensity, and we observe the opposite when using the 50X objective. The signal response has great homogeneity for both APTMS and DETA compared to Klarite and indirectly confirming the uniform distribution of the SERS hotspots.

The same samples used for the homogeneity study have been cleaned by 30 min UV O$_3$ treatment, and the SERS measurements, made afterward, demonstrate that the MBA has been completely removed. A new cycle of measures with MBA SAM has given the same results as before, demonstrating that the substrate is very stable and can be reused for more measurements by a simple cleaning procedure.

3.5. SERS detection of 3-methylindole (Skatole)

After optimizing the growth time and deposition processes assessed as described above, SERS signals of 3-methylindole (Skatole) solutions in the concentration range between (1 nM − 10 μM) were measured to evaluate the analytical performances. Previously cleaned by UV-O$_3$

treatment, substrates were immersed for one hour in solutions containing 3-methylindole at increasing concentrations and rapidly washed in ethanol. We decided to deposit the analyte by immersion instead of via the drop-casting method to avoid the well-known coffee ring effect that may lead to a less uniform SERS response. The Raman signal was measured from different points of the substrate at each concentration. Especially at the lowest concentrations, there are very few molecules of the analyte on the substrate. A significant number of measurements were needed to make a statistic and demonstrate the high sensitivity that the substrate allows.

Fig. 6 resumes the analytical performances of the substrate. For both substrates (APTMS and DETA), the relation between Skatole concentration and Raman signal is linear against a logarithmic axis for the concentration. The equation describing the substrate fabricated using APTMS is ($y = 0.136\ x\ + 0.800$), with $R^2 = 0.989$. Similarly, the linear fitting equation for the DETA-based substrate is ($y = 0.033\ x\ + 3.091$), with $R^2 = 0.969$. The analyzed concentration range includes the accepted threshold levels for Skatole, within the range of 0.5–1 μg/ml (1.8–3.6 μM), indicating that the proposed system can detect 3-methylindole at concentrations well below the ones at which the human being is sensitive. These results have been compared with Skatole signal with Klarite, where at a Skatole concentration of 100 μM the Raman signal is as low as 0.94 counts/(W s) for the most intense peak (Figure S7-S8). The estimated limit of detection (LOD) and limit of quantification (LOQ) for the sensors prepared with the different silanes are reported in Table 3 and shows for both APTMS and DETA a LOD in the part-per-trilion range, achieving 42.2ppt for APTMS, orders of magnitude better than what is required by practical applications. In Figure S6 of SI, we compare SERS signals obtained for 10 μM Skatole solution deposited on Klarite, APTMS 2.5 %, and DETA 4 %.

4. Conclusions

The efficiency of a SERS substrate is strongly correlated to the density of hotspots. A highly responsive and uniform substrate is needed to detect biomolecules at low concentrations. The optimization approach demonstrated in this work allows for the design and fabrication of gold

Table 3

Detection limit and quantification for DETA and APTMS SERS substrates.

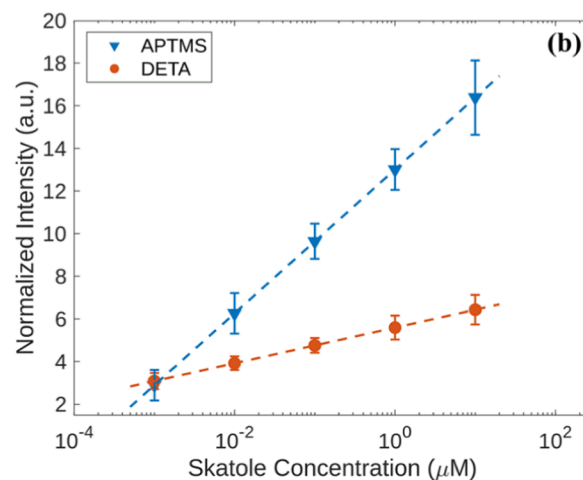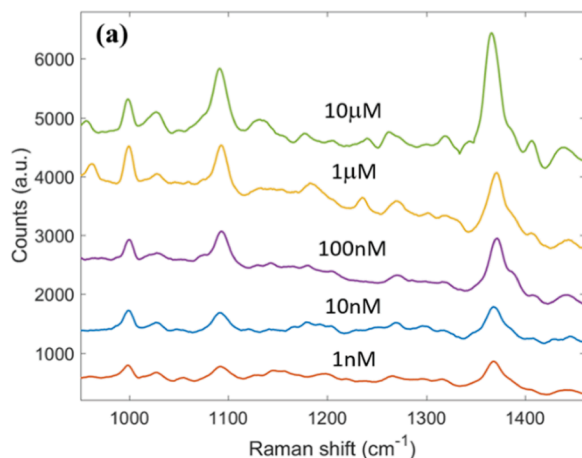| Substrate	LOD (nM)	LOD (ppt)	LOQ (nM)	LOQ (ppt)
APTMS	0.32	42.2	0.98	129.1
DETA	2.22	292.4	6.67	878.7

Fig. 6. (a) Raman spectra for Skatole at different concentrations obtained on the APTMS substrate. (b) Calibration curves for Skatole detection on APTMS and DETA substrates.

grown nanostructured surfaces (GNSs) performing as highly optimized and uniform SERS substrates whose efficiencies are maximized for a chosen excitation wavelength and Raman shift by design. Such design is based on an electromagnetic simulation to determine the optimal particle center-to-center distance and an ERSA simulation to determine the seed deposition conditions that are required to obtain such spatial arrangement of nanoparticles. We have employed a simple wet-chemical bottom-up approach to fabricating centimeter-scale substrates with high SERS sensitivity and excellent uniformity of the SERS signal. In fact, deviations in SERS response tested with MBA were as low as 1.3 % for the highest magnification. This fabrication methodology can be helpful in cheap label-free immunoassays and biosensors and quick detection of hormones that are key in areas such as agri-food industries. As a demonstration of the obtained SERS substrates, we detected Skatole in concentrations down to 1 nM, which is at least 1000-fold lower than the level currently used as a reference in food industry processes. Our best results were obtained with APTMS-functionalized substrates, whose estimated limit of detection was 320 pM, corresponding to 42.2 parts per trillion.

CRediT authorship contribution statement

Matteo Giardino: Conceptualization, Investigation, Validation, Visualization, Data curation, Writing – original draft, Writing – review & editing, Formal analysis, Software. **Ilaria Mannelli:** Conceptualization, Investigation, Data curation, Writing – original draft, Writing – review & editing, Formal analysis. **Renwen Yu:** Conceptualization, Data curation, Writing – original draft, Writing – review & editing, Formal analysis, Software. **F. Javier García de Abajo:** Conceptualization, Supervision, Software, Writing – original draft, Writing – review & editing, Resources. **Valerio Pruneri:** Conceptualization, Supervision, Writing – original draft, Writing – review & editing, Resources. **Davide Janner:** Conceptualization, Data curation, Writing – original draft, Writing – review & editing, Formal analysis, Software, Investigation, Resources, Project administration, Supervision.

Declaration of Competing Interest

The authors declare that they have no known competing financial interests or personal relationships that could have appeared to influence the work reported in this paper.

Data availability

The data that has been used is confidential.

Acknowledgments

Appendix A. Supplementary data

Supplementary data to this article can be found online at https://doi.org/10.1016/j.apsusc.2023.159076.

References

[1] L. Yao, L. Ouyang, J. Lv, P. Dai, L. Zhu, Microchem. J. 166 (2021), 106221.
[2] K. Wang, J. Li, Spectrochim. Acta A Mol. Biomol. Spectrosc. 263 (2021), 120218.
[3] D.S. Moore, P.U. Jepsen, K. Volka, in: Handbook of Spectroscopy, Wiley-VCH Verlag, GmbH & Co. KGaA, 2014, pp. 1037–1078.
[4] M. Zhang, X. Li, J. Pan, Y. Zhang, L. Zhang, C. Wang, X. Yan, X. Liu, G. Lu, Biosens. Bioelectron. 190 (2021), 113421.
[5] W. Qi, D. Shaowei, H. Karl, Y. Chenxu, in: Proceedings International Conference of Agricultural Engineering, Zurich, 2014, p. C0086.
[6] M. Moskovits, J. Chem. Phys. 69 (1978) 4159–4161.
[7] R.M. Hexter, M.G. Albrecht, Spectrochim. Acta A: Mol. Spectrosc. 35 (1979) 233–251.
[8] K. Kneipp, Y. Wang, H. Kneipp, L.T. Perelman, I. Itzkan, R.R. Dasari, M.S. Feld, Phys. Rev. Lett. 78 (1997) 1667–1670.
[9] Y. Wang, J. Irudayaraj, Philos Trans R Soc Lond B Biol Sci 368 (2013) 20120026.
[10] H.-K. Choi, K.S. Lee, H.-H. Shin, J.-J. Koo, G.J. Yeon, Z.H. Kim, Acc. Chem. Res. 52 (2019) 3008–3017.
[11] Y. Qiu, C. Kuang, X. Liu, L. Tang, Sensors 22 (2022) 4889.
[12] E. Hao, G.C. Schatz, J. Chem. Phys. 120 (2004) 357–366.
[13] D.-K. Lim, K.-S. Jeon, H.M. Kim, J.-M. Nam, Y.D. Suh, Nat. Mater. 9 (2010) 60–67.
[14] A. Lee, G.F.S. Andrade, A. Ahmed, M.L. Souza, N. Coombs, E. Tumarkin, K. Liu, R. Gordon, A.G. Brolo, E. Kumacheva, J. Am. Chem. Soc. 133 (2011) 7563–7570.
[15] M. Moskovits, Nature 464 (2010) 357.
[16] M. Fleischmann, P.J. Hendra, A.J. McQuillan, Chem. Phys. Lett. 26 (1974) 163–166.
[17] A. Campion, P. Kambhampati, Chem. Soc. Rev. 27 (1998) 241–250.
[18] B. Pettinger, U. Wenning, H. Wetzel, Surf. Sci. 101 (1980) 409–416.
[19] J.A. Dieringer, A.D. McFarland, N.C. Shah, D.A. Stuart, A.V. Whitney, C.R. Yonzon, M.A. Young, X. Zhang, R.P.V. Duyne, Faraday Discuss. 132 (2006) 9–26.
[20] C.L. Haynes, A.D. McFarland, R.P.V. Duyne, Anal. Chem. 77 (2005), 338 A-346 A.
[21] J. Liu, Z. Wang, Y. Meng, C. Chen, Q. Chen, Y. Wang, S. Dou, X. Liu, N. Lu, Talanta 258 (2023), 124408.
[22] L. Hou, M. Shao, Z. Li, X. Zhao, A. Liu, C. Zhang, X. Xiu, J. Yu, Z. Li, Opt. Express, OE 28 (2020) 29357–29367.
[23] L.A. Lane, X. Qian, S. Nie, Chem. Rev. 115 (2015) 10489–10529.
[24] J.F. Betz, W.W. Yu, Y. Cheng, I.M. White, G.W. Rubloff, Phys. Chem. Chem. Phys. 16 (2014) 2224–2239.
[25] J. Chen, Y. Li, K. Huang, P. Wang, L. He, K.R. Carter, S.R. Nugen, A.C.S. Appl, Mater. Interfaces 7 (2015) 22106–22113.
[26] G. Das, E. Battista, G. Manzo, F. Causa, P.A. Netti, E. Di Fabrizio, ACS Appl. Mater. Interfaces (2015).
[27] A. Dandapat, T.K. Lee, Y. Zhang, S.K. Kwak, E.C. Cho, D.-H. Kim, A.C.S. Appl, Mater. Interfaces 7 (2015) 14793–14800.
[28] K. Milenko, F.T. Dullo, P.C.V. Thrane, Z. Skokic, C.A. Dirdal, Nanomaterials 13 (2023) 1598.
[29] S. Mahajan, R.M. Cole, B.F. Soares, S.H. Pelfrey, A.E. Russell, J.J. Baumberg, P. N. Bartlett, J. Phys. Chem. C 113 (2009) 9284–9289.
[30] M.E. Hankus, D.N. Stratis-Cullum, P.M. Pellegrino, In (2011).
[31] X. Ma, L. Jiang, X. Li, B. Li, J. Huang, J. Sun, Z. Wang, Z. Xu, L. Qu, Y. Lu, T. Cui, Microsyst Nanoeng 5 (2019) 1–10.
[32] C. Sun, S. Zhang, J. Wang, F. Ge, Surf. Interfaces 28 (2022), 101616.
[33] K. Khabarov, E. Filalova, M. Nouraldeen, E. Kameneva, A. Musaev, S. Tikhonov, V. Ivanov, Nanomaterials (basel) 13 (2023) 812.
[34] N. Félidj, J. Aubard, G. Lévi, J.R. Krenn, A. Hohenau, G. Schider, A. Leitner, F. R. Aussenegg, Appl. Phys. Lett. 82 (2003) 3095–3097.
[35] V. Joseph, A. Matschulat, J. Polte, S. Rolf, F. Emmerling, J. Kneipp, J. Raman Spectrosc. 42 (2011) 1736–1742.
[36] S. Hong, X. Li, J. Nanomaterials 2013 (49) (2013) 49.
[37] P. Pal, A. Bonyár, M. Veres, L. Himics, L. Balázs, L. Juhász, I. Csarnovics, Sens. Actuators, A 314 (2020), 112225.
[38] J. Eklöf, T. Gschneidtner, S. Lara-Avila, K. Nygård, K. Moth-Poulsen, RSC Adv. 6 (2016) 104246–104253.
[39] Z. Adamczyk, P. Weroński, Adv. Colloid Interface Sci. 83 (1999) 137–226.
[40] J. Leong, P.C.H. Morel, R.W. Purchas, B.H.P. Wilkinson, Meat Sci. 88 (2011) 45–50.
[41] J.-M. Maesa, F.-X. Muñoz-Pascual, E. Baldrich, Analyst 138 (2013) 1346–1352.
[42] J.-E. Haugen, C. Brunius, G. Zamaratskaia, Meat Sci. 90 (2012) 9–19.
[43] K.M. Sørensen, S.B. Engelsen, J. Agric. Food Chem. 62 (2014) 9420–9427.
[44] G.A. Niklasson, C.G. Granqvist, O. Hunderi, Appl. Opt,, AO 20 (1981) 26–30.
[45] A. Sousa-Castillo, Ó. Ameneiro-Prieto, M. Comesaña-Hermo, R. Yu, J.M. Vila-Fungueiriño, M. Pérez-Lorenzo, F. Rivadulla, F.J. García de Abajo, M.A. Correa-Duarte, Nano Energy 37 (2017) 118–125.
[46] P.B. Johnson, R.W. Christy, Phys. Rev. B 6 (1972) 4370–4379.
[47] F.J. García de Abajo, A. Howie, Phys. Rev. B 65 (2002), 115418.
[48] R.H. Perry, D.W. Green (Eds.), Perry`s Chemical Engineers` Handbook, 8th ed, McGraw-Hill, New York, 2008.
[49] J. Hu, W. Li, J. Chen, X. Zhang, X. Zhao, Surf. Coat. Technol. 202 (2008) 2922–2926.
[50] C. for D.E. and Research, U.S. Food and Drug Administration (2021).
[51] R. Esteban, A.G. Borisov, P. Nordlander, J. Aizpurua, Nat Commun 3 (2012) 825.
[52] M. Semmler, J. Rička, M. Borkovec, Colloids Surf A Physicochem Eng Asp 165 (2000) 79–93.
[53] K.C. Grabar, P.C. Smith, M.D. Musick, J.A. Davis, D.G. Walter, M.A. Jackson, A. P. Guthrie, M.J. Natan, J. Am. Chem. Soc. 118 (1996) 1148–1153.
[54] L. Finegold, J.T. Donnell, Nature 278 (1979) 443–445.
[55] Y.A.D. Fernandez, T.A. Gschneidtner, C. Wadell, L.H. Fornander, S.L. Avila, C. Langhammer, F. Westerlund, K. Moth-Poulsen, Nanoscale 6 (2014) 14605–14616.

[56] J. Sukham, O. Takayama, A.V. Lavrinenko, R. Malureanu, A.C.S. Appl, Mater. Interfaces 9 (2017) 25049–25056.

[57] P.K. Jain, K.S. Lee, I.H. El-Sayed, M.A. El-Sayed, J. Phys. Chem. B 110 (2006) 7238–7248.

[58] K. Esashika, R. Ishii, S. Tokihiro, T. Saiki, Opt. Mater. Express, OME 9 (2019) 1667–1677.

[59] L. Chen, H. Sun, Y. Zhao, Y. Zhang, Y. Wang, Y. Liu, X. Zhang, Y. Jiang, Z. Hua, J. Yang, RSC Adv. 7 (2017) 16553–16560.